Synthesis, characterization, photocatalytic effect of thiourea and thioglycolic acid on ZnO/CuS nanocomposites for degradation of Mordant black 11 dye

S. Sharon Tamil Selvi[1] · G. Hannah Priya[1] · A. Alinda Shaly[1] · L. Allwin Joseph[2] · J. Mary Linet[1]

Abstract

ZnO/CuS nanocomposite was synthesized by hydrothermal technique using two different sulfur source such as TU = thiourea and TA = thioglycolic acid. Pure ZnO and CuS (TU and TA) nanoparticles were synthesized, and a comparative analysis was performed. X-ray diffraction discloses the average crystalline size of the ZnO/CuS (TU and TA) to be 18 nm and 12 nm, respectively. HR-TEM exhibits a particle size of 27.50 nm and 30.50 nm for ZnO/CuS (TU) and ZnO/CuS (TA). Brunauer–Emmett–Teller analysis confirms the surface area of ZnO/CuS (TU) to be 1.246 m^2/g and ZnO/CuS (TA) to be 11.086 m^2/g. The band gaps were estimated to be 3.1 eV for ZnO/CuS (TU) and 1.6 eV and 2.64 eV for ZnO/CuS (TA). The photocatalytic activity of ZnO, ZnO/CuS (TU) and ZnO/CuS (TA) nanocomposites was investigated by the solar irradiation of mordant black 11 dye in an aqueous medium.

Keywords ZnO/CuS nanocomposite · Hydrothermal method · HRTEM · Optical properties · Photocatalytic property · Mordant black 11

1 Introduction

Over the past few years, nanotechnology has gained enormous popularity due to its functionality in diverse fields ranging from energy to environmental applications. The chemical, physical, electronic, magnetic and surface properties of nanoparticles differ greatly when compared to its bulk equivalent. Transition metal complexes such as Zn, Cd, Cu, TiO_2, Ni, Fe and Co have gained much interest in the field of research due to its use in electronic and photonic devices [1–4]. Among the sulfide-based semiconductors, CuS is a p-type semiconductor that has been used in solar cells [5], photocatalysis [6], chemical sensors [7], optical filters [8], etc. CuS has a narrow band gap of 1.2–2.2 eV that is suitable for solar light dye degradation. While a CuS nanoparticle (NPs) is a good photocatalytic material, they are susceptible to corrosion under sunlight. This photocorrosion is prevented by adding ZnO to the CuS NPs. ZnO NPs act as an encapsulating shell over the CuS NPs and prevent it from getting oxidized [9, 10]. ZnO is a n-type semiconductor having a wide band gap of ~ 3.6 eV. It has been exploited in areas such as rubber, paint, coating and cosmetics. Due to its wide band gap, it can be utilized only in UV region and the sun provides only 5% of it. ZnO NPs has a large band gap, lower quantum efficiency, and high recombination of photoinduced electron–hole pairs which has led to the limitations in its wide applications [11–13]. Thus, the inadequacy of both CuS and ZnO was eradicated when they were combined to form a ZnO/CuS nanocomposite. ZnO/CuS nanocomposites, when compared with pure ZnO and CuS, possess better physicochemical properties and improved sensing capabilities [14, 15].

Yu et al. [16] fabricated CuS/ZnS nanocomposites to degrade rhodamine B dye which is resistant to biodegradation and direct photolysis. Hollow spheres of diameter 225 nm were synthesized between ZnS solid spheres and Cu^{2+} ions in the mixture by ion-exchange synthesis method. CuS NPs were grown on ZnO nanowires hydrothermally by a successive ionic layer adsorption and reaction (SILAR) method, where the ZnO/CuS nanowire array revealed a

✉ J. Mary Linet
   linet.mary@gmail.com

1   Department of Physics, Loyola College, Chennai 600034, India

2   Department of Physics, The New College, Chennai 600014, India

superior photocatalytic activity under visible light compared to pure ZnO and CuS NPs. The interfacial charge transfer process from the valence band of ZnO to CuS helped in charge separation and reduction in recombination rate [17]. Liu et al. synthesized a ZnO/CuS core/shell nanoarrays for solar cell applications by hydrothermal and ion exchange method. The prepared CuS shells of 5–30 nm thickness were made to deposit onto the ZnO nanorods arrays. The constructed solar cell produced an efficiency of 1.02% [18]. By combining ZnO to CuS NPs, the composite showed an enhanced absorption characteristics and a broadened visible light response [19]. Hong et al. fabricated a CuS/ZnO nanowire array using a stainless steel mesh. The ZnO nanowire array was grown on the steel mesh containing a ZnO seed layer. Further, CuS NPs were deposited onto the ZnO nanowire array by successive ionic layer adsorption and reaction (SILAR) method. The band gap of ZnO/CuS nanocomposite was 2.39 eV, and they displayed a strong absorption peak in the visible light and near-IR region. ZnO/CuS heterostructured nanoarrays were widely used in piezo-photocatalytic activity for the degradation of methylene blue dye [20].

Thus, a p–n heterostructured nanocomposite of ZnO/CuS was synthesized by one-pot hydrothermal process, which has an enhanced mordant black 11 dye photodegradation activity under solar light when compared to CuS and ZnO nanoparticles. ZnO/CuS nanocomposite was prepared by utilizing two sulfur ion sources thiourea (TU) and thioglycolic acid (TA), and their properties were investigated. Hydrothermal method is considered to be efficient, because it is demonstrated to be effective for controlling the shape and size of ZnO/CuS nanocomposites. The present work emphasizes that CuS could remarkably improve the visible light photocatalytic activity of ZnO using two different sulfur sources. Therefore, the process of improving solar light-induced degradation of ZnO/CuS nanocomposite has been discussed in detail in this work.

2 Experimental details

2.1 Materials

Copper acetate monohydrate $[Cu(CH_3COO)_2]$, zinc acetate $[Zn(CH_3COO)_2 \cdot (H_2O)_2]$, sodium hydroxide (NaOH), thiourea (CH_4N_2S), thioglycolic acid $(C_2H_4O_2S)$, mordant black 11 and ethanol were used as obtained from Merck. The solvent utilized in all the experimental procedures was deionized water.

2.2 Preparation of ZnO, CuS and ZnO/CuS nanocomposites

70 ml of distilled water was employed to dissolve 5 g of zinc acetate, and to this solution, 0.65 M of NaOH was added slowly in drops. After ceaseless stirring for 2 h, the reaction mixture was poured into a 100-ml steel autoclave with an inner coating made of Teflon and was subjected to hydrothermal treatment for 180 °C for 12 h. The white precipitate obtained was cleansed and separated by centrifuging 4 times with distilled water and ethanol. Zinc oxide nanoparticles were prepared by drying the obtained sample in a vacuum oven at 70 °C for 10 h.

Through constant stirring, 0.5 M of copper acetate monohydrate was dissolved in 20 ml of distilled water. 2.5 g of thiourea (sulfur source) was added to the above solution. 0.16 M of NaOH was dissolved drop by drop to maintain the pH value. The prepared solution immediately turned greenish black. In order to enable proper mixing, the solution was repeatedly stirred for 5 h. The above formulated solution was poured into a stainless steel Teflon-lined autoclave of 100-ml quantity, and then kept in a furnace at a temperature of 180 °C for 8 h and slowly cooled down. The obtained precipitate was finally centrifuged with ethanol and deionized water. The resultant was then dried at 70 °C for 4 h in vacuum. The sample was annealed at 150 °C for 4 h to improve ordering. The similar procedure was repeated again with the addition of thioglycolic acid (1 ml) instead of thiourea as the sulfur source. Thus, nanoparticles of CuS (A2 and A4) were synthesized from two different sulfur sources thiourea and thioglycolic acid.

0.5 g of the prepared ZnO NPs and CuS NPs prepared using thiourea were dispersed in 20 ml of deionized water in two beakers separately under an ultrasonic bath. After 30 min, the solutions were combined and stirred magnetically. After 60 min, light brown-colored solution was obtained as a result of the formation of the ZnO/CuS nanocomposite. The final solution was poured into a 150-ml Teflon-coated stainless steel autoclave and was kept in a furnace to undergo hydrothermal treatment at 180 °C for 10 h. In the end, the obtained ZnO/CuS (A3) nanocomposite was centrifuged and cleaned repeatedly with water and ethanol and then dried at 150 °C for 10 h. The similar procedure was repeated using CuS synthesized using thioglycolic acid, and ZnO/CuS nanocomposite (A5) was obtained.

The synthesized ZnO, CuS and ZnO/CuS nanocomposites are denoted as A1–A5: A1 = ZnO; A2 = CuS(TU); A3 = ZnO/CuS (TU); A4 = CuS (TA) and A5 = ZnO/CuS (TA).

3 Results and discussion

3.1 X-ray diffraction (XRD) analysis

The XRD patterns of CuS (A2 and A4), ZnO/CuS nanocomposites (A3 and A5) and ZnO nanoparticles (A1) are rendered in Fig. 1. The lattice planes (101), (102), (006), (107) and (201) indicate the formation of hexagonal CuS, Fig. 1a, d as per the JCPDF NO. 06–0464 [15]. The crystal planes (100), (002), (101), (110), (103), (200), (112) and (201) for ZnO in the diffractogram can be correlated to the formation of hexagonal phase with cell constants $a = 3.253$ Å and $c = 5.277$ Å (JCPDF NO. 36-1451) [21].

The average crystallite sizes of CuS (A2 and A4), ZnO nanoparticles (A1) and ZnO/CuS nanocomposites (A3 and A5) were estimated using Scherrer's equation [22]

$$D = \frac{k\lambda}{\beta \mathrm{Cos}\theta} \tag{1}$$

where k stands for the Scherrer constant or shape factor of the average crystallites and is presumed to have a value of 0.9, D relates to the crystallite size, λ pertains to the wavelength of X-ray Cu Kα radiation (1.5406 Å), β designates the full width half maximum (FWHM) in radians of the respective peaks and θ depicts the Braggs diffraction angle in degrees.

The approximate average crystallite size of ZnO nanoparticles (A1) was observed to be 38.84 nm. The average crystallite size of CuS NPs (A2 and A4) was estimated as 29 nm and 24 nm, respectively. As shown in Fig. 1c, e, all the diffraction peaks for CuS are retained in the diffractogram for the ZnO/CuS composites. It clearly reveals that the structure and crystalline phases of isolated CuS NPs are retained even after they are grown onto ZnO NPs. The strong peaks in XRD prove the crystalline nature of the samples. Structural transformation of either ZnO or CuS was not observed. In addition, there were no XRD peaks observed referring to any intermediate compound formation. The average crystallite size was calculated from FWHM of major XRD peaks using Scherrer's formula [20].

According to the calculation, the average crystallite size of the ZnO/CuS nanocomposites (A3 and A5) was found to be about 18 nm and 12.81 nm, respectively. The crystallite size estimated from Scherrer's formula is found to decrease when CuS is composed with ZnO nanoparticles. The decrease in crystallite size correlates with a large developed surface of grain boundaries, thus leading to a larger scattering effect. Another reason for the decreased crystallite size values may be due to the drag force exerted by the ZnO on boundary motion and grain growth.
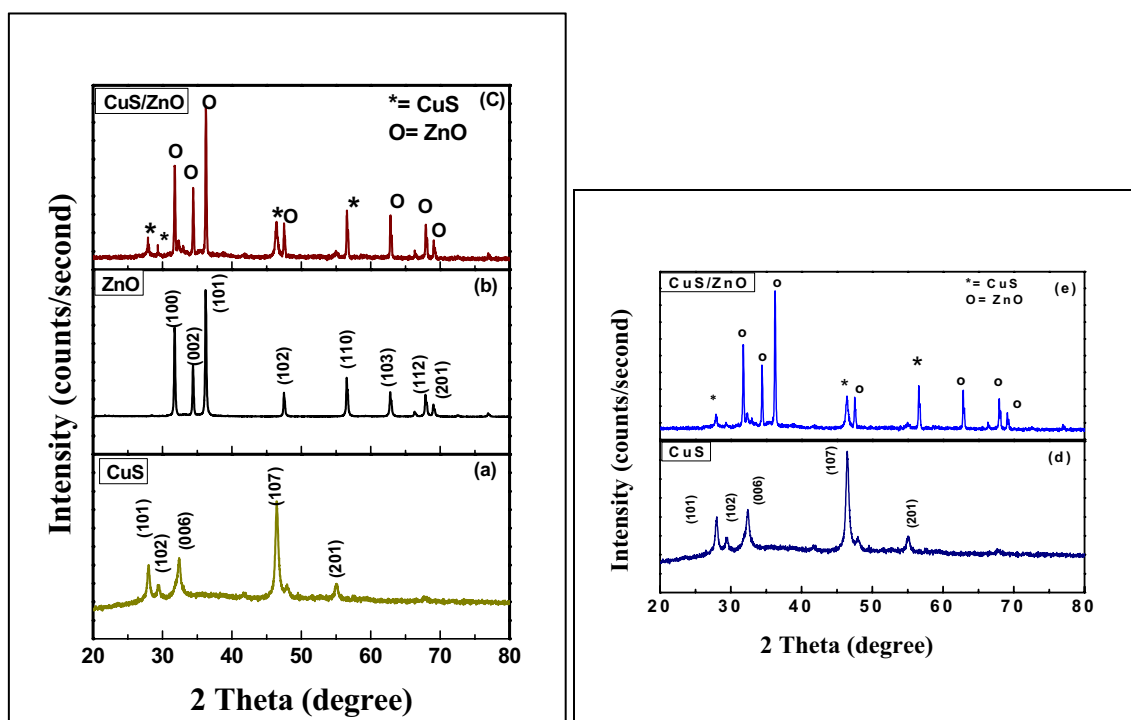

Fig. 1 XRD patterns of samples: (a) CuS (A2) (b) ZnO (A1) (c) ZnO/CuS (A3) (d) CuS (A4), and (e) ZnO/CuS (A5)

3.2 HRTEM and EDAX analysis

Figure 2 represents the electron-dispersive X-ray spectroscopy (EDAX) analysis of ZnO/CuS nanocomposite which confirms the presence of the elements Cu, S, Zn and O in the sample. The high purity of the prepared sample was verified by the nonexistence of any other elemental peaks.

Morphological investigations of A1, A2, A3, A4 and A5 were made by HRTEM estimations, and the acquired outcomes are shown in Fig. 3. It can be noticed that the morphologies and sizes of the prepared nanoparticles exceptionally rely upon the applied conditions. The existence of the remaining acetate ligands in ZnO nanoparticles is unable to maintain the stabilization which leads to the effect of agglomeration in A1 nanoparticles. The obtained ZnO/CuS (A3) nanocomposite in Fig. 3h shows hexagonal morphology which is in concurrence with XRD patterns. A slight tendency of agglomeration, due to the small dimensions and high surface energy in the image of ZnO (A1) composed with CuS (A4), is shown in Fig. 3n. Further, washing the remaining acetate ligands is unable to maintain the stabilization against agglomeration of the ZnO nanoparticles. Additional information about the microstructures of the ZnO NPs, CuS and ZnO/CuS nanocomposite is given by their SAED patterns and HRTEM images. The SAED patterns for all the samples are presented with their TEM images in Fig. 3c, f, i, l, o, and the circular ring pattern with vivid diffraction pattern spots validates the polycrystalline wurtzite phase of the material. The diffraction planes got from the SAED patterns coordinate well with the XRD patterns. HRTEM images show the structurally uniform lattice fringes of nanoparticles, Fig. 3a, d, g, j, m, suggesting the good crystalline nature of the prepared materials. The HRTEM investigations of an individual ZnO show a single crystal nature and growth direction along c-axis. When ZnO is incorporated with CuS, a set of lattice planes were formed on the surface, revealing the polycrystalline CuS nanoparticles that leads to the change in morphology. The measured fringes spacing of A1 is 0.19 nm, A2 is 0.34 nm, A3 is 0.26 nm, A4 is 0.30 nm and A5 is 0.22 nm and 0.30 nm. The particle size of A2, A3, A4 and A5 was found to be 27.20 nm, 22.47 nm, 30.10 nm and 20.54 nm respectively.

3.3 Particle size determination

The particle size distributions of the synthesized pure CuS and ZnO/CuS nanocomposite were studied by XRD and TEM analysis. Figure 1 shows the XRD peaks of CuS and ZnO/CuS nanocomposite, respectively. Figure 4 shows the particle size distribution histogram of pure CuS and ZnO/CuS nanocomposite using HRTEM which reveals spherical nanoparticles. The average particle sizes as observed from the TEM images are similar to the consequences of XRD estimations for CuS and ZnO/CuS [17]. The average crystallite size derived from the Scherrer analysis is concordant with the values got from HRTEM analysis as furnished in Table 1.

3.4 Brunauer–Emmett–Teller (BET) analysis

The surface area and the pore size of pure ZnO (A1) and ZnO/CuS nanocomposites (A3 and A5) were obtained by
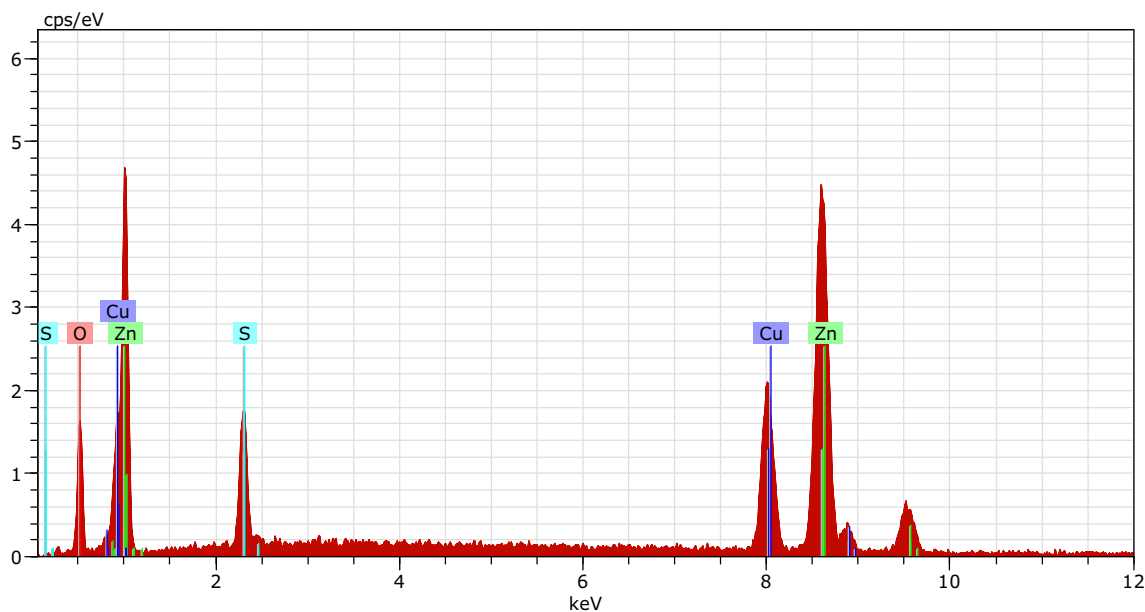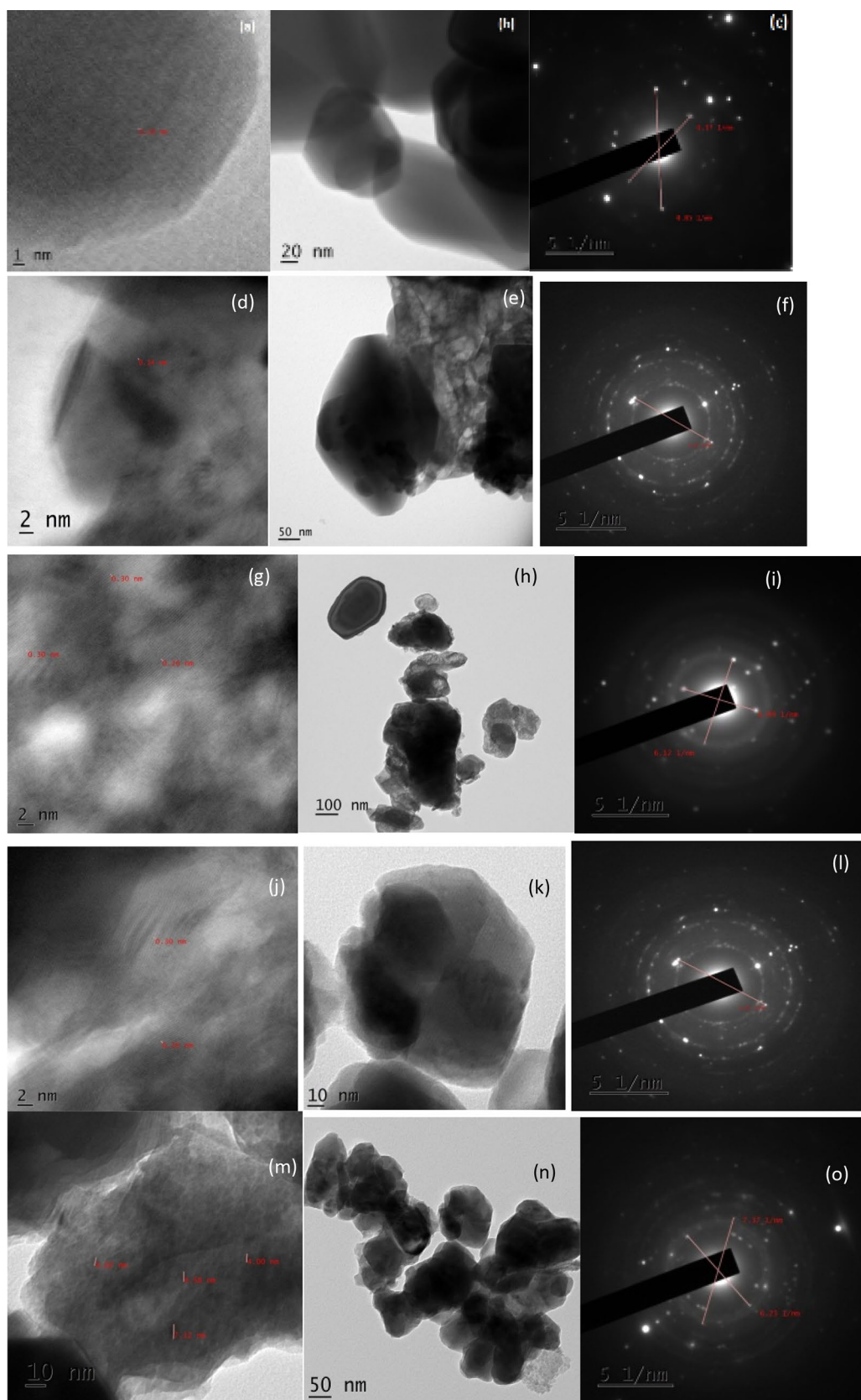

Fig. 2 EDAX spectrum of ZnO/CuS nanocomposite

Fig. 3 HR-TEM images of A1, A2, A3, A4 and A5 nanoparticles (**a**, **d**, **g**, **j**, **m**), their relevant TEM images (**b**, **e**, **h**, **k**, **n**) and SAED patterns (**c**, **f**, **i**, **l**, **o**)
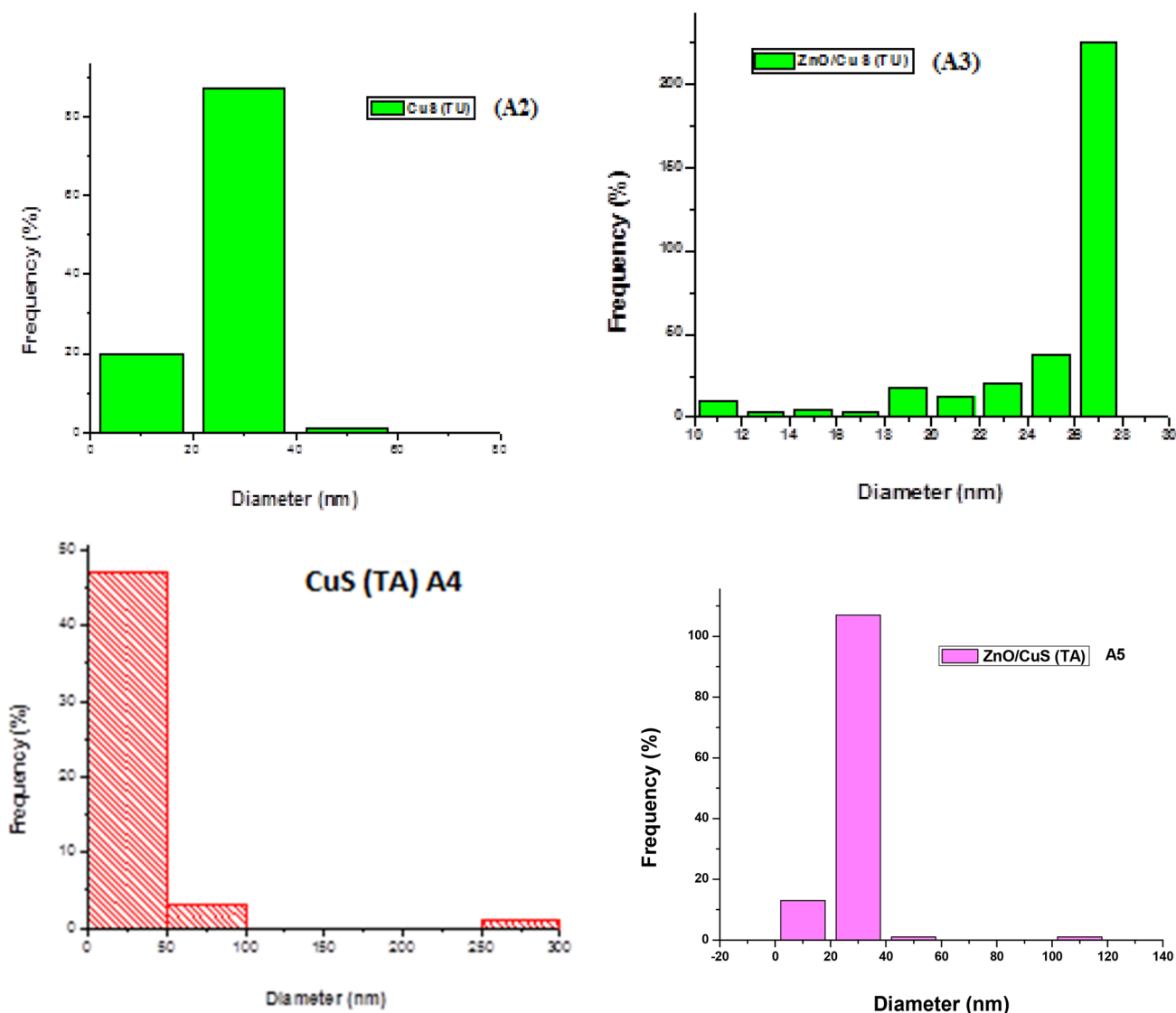
Fig. 4 Particle size distribution analyses of CuS and ZnO/CuS nanocomposite

Table 1 Calculated crystallite size and average crystallite sizes obtained from the Scherrer analysis, DLS and HRTEM analysis of CuS and ZnO/CuS nanocomposite

Samples	Average particle size (nm)	
	Scherrer analysis	HRTEM analysis
A2	29	27.20
A3	18	22.47
A4	24	30.10
A5	13	20.54

nitrogen adsorption–desorption isotherms as depicted in Fig. 5. According to the Brunauer–Deming–Deming–Teller categorization, the nanoparticles showed type IV isotherm, where the area of hysteresis loop specifies the existence of mesoporous structure. The surface area of ZnO/CuS nanocomposite (A5) obtained from BET analysis shows a greater surface area when compared to A1 and A3. The larger surface area offers increased surface active sites for the adsorption of the reactive molecules and is estimated to be useful in the photocatalytic method [23, 24]. These significances provide evidence to the improved photocatalytic performance of ZnO/CuS nanocomposite (A5).

3.5 UV Diffused reflectance spectral analysis

The UV–Vis spectra of the ZnO NPs (A1), CuS (A2), ZnO/CuS (A3), CuS (A4) and ZnO/CuS (A5) nanocomposite were recorded to evaluate the light harvesting abilities of the samples; these are shown in Fig. 6. The optical absorbance
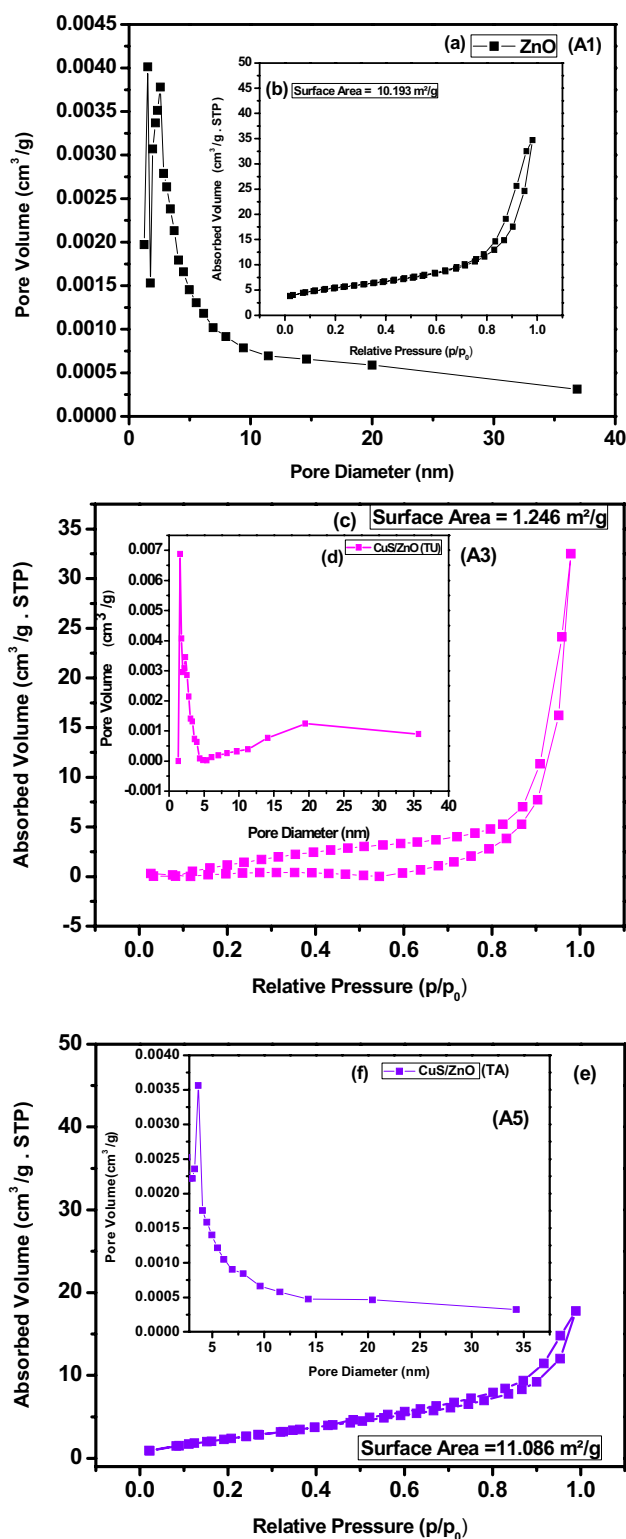
Fig. 5 Nitrogen adsorption–desorption isotherms for (a) A1 and (c, e) A3 and A5 at 77.4 K. (inset: (b, d, f) the respective pore size distribution)

in terms of Kubelka–Munk function was estimated using the equation:

$$F(R) = \frac{\left(1 - R^2\right)}{2R} \tag{2}$$

where R denotes the diffuse reflectance. The reflectance spectra for these samples are plotted in the wavelength range of 200–1000 nm. Figure 6 insets represent the Kubelka–Munk plot for ZnO NPs (A1), CuS NPs (A2 and A4) and ZnO/CuS (A3 and A5) composite, where plotting $(F(R)h\nu)^2$ versus $h\nu$ is used to determine the band gap of the materials. The value of E_{phot} extrapolated to $F(R)E = 0$ provides an absorption energy which is relative to a band gap E_g. The estimated band gap energy for ZnO NPs (A1) was found to be 3.38 eV, 1.76 eV and 1.5 eV which correspond to the individual band gaps of CuS (A2 and A4) NPs, respectively. The band gap of ZnO/CuS nanocomposite (A3) was found to be 3.1 eV and ZnO/CuS (A5) is 1.6 eV and 2.64 eV, respectively. These values demonstrated that the obtained samples exhibit strong absorption in both UV and visible light regions. Pure ZnO has a wide band gap which cannot absorb the visible area of the solar spectrum (> 420 nm); therefore, the grouping up of ZnO with CuS NPs forms a CuS/ZnO nanocomposite which has an increased level of visible light absorption caused by the presence of CuS NPs [25, 26]. Thereby, the rise of CuS composition in the CuS/ZnO nanocomposite led to an increased amount of absorption, which in turn improved its photocatalytic activity. This is mainly due to the CuS modification which brought an increase in the surface electric charge of ZnO in the nanocomposite; thus, it leads to a change in the fundamental process of electronic transfer during the irradiation [27, 28].

3.6 Fourier Transform Infrared (FTIR) analysis

The obtained chemical bonds in ZnO, CuS and ZnO/CuS nanoparticles were studied by the FT-IR spectra. As displayed in Fig. 7, 3530 cm^{-1} and 1613 cm^{-1} exhibited an O–H peak that occurs as a result of the absorption of the water molecules. The stretching vibration of C–O bond is the reason behind the origin of the peak at 1076 cm^{-1}. The peaks ranging from 400 to 720 cm^{-1} were recognized as Cu–S and Zn–O bonds and they confirm the formation of metal–sulfur bond. Thus, ZnO/CuS nanocomposite is formed.

3.7 Photoluminescence spectral analysis

The peaks of ZnO and CuS NPs were observed in the PL spectra of as–obtained ZnO/CuS nanocomposites as portrayed in Fig. 8. The photoluminescence spectrum of the ZnO NPs (A1) was recorded by utilizing an excitation wavelength of 320 nm at room temperature. A weak emission
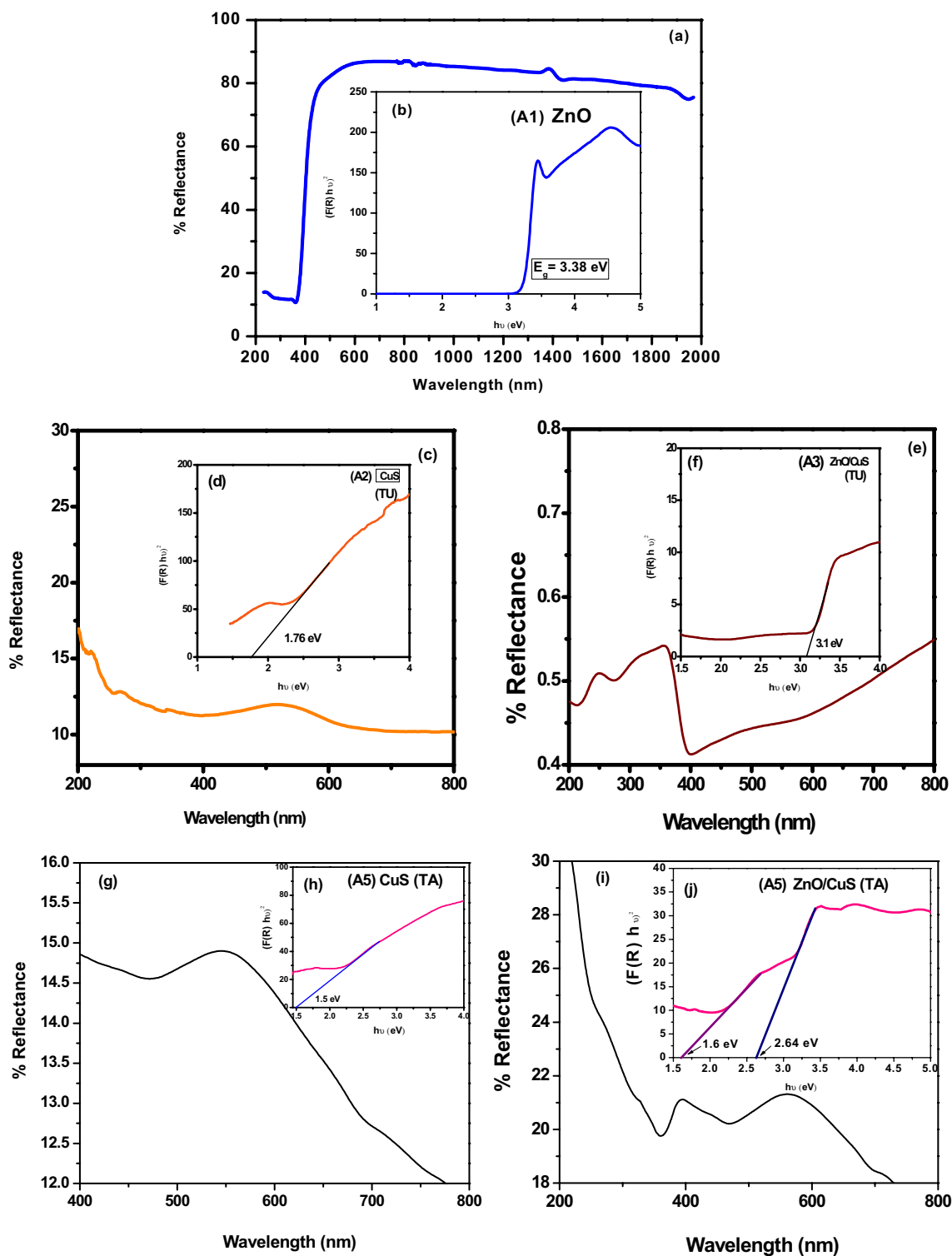
Fig. 6 UV–Vis reflectance spectra and Kubelka–Munk function of A1, A2, A3, A4 and A5 for obtaining the band gap energy from the variation of $(F(R)h\nu)^2$ with photon energy $(h\nu)$

peak near 380 nm can be correlated to the phenomenon of recombination between the conduction and valence bands. The strong intrinsic defect peak near 420 nm is due

to oxygen and zinc vacancies. The PL spectra of CuS NPs (A4) showed the absence of a clear absorption peak, which may be due to the broad distribution size of CuS and strong
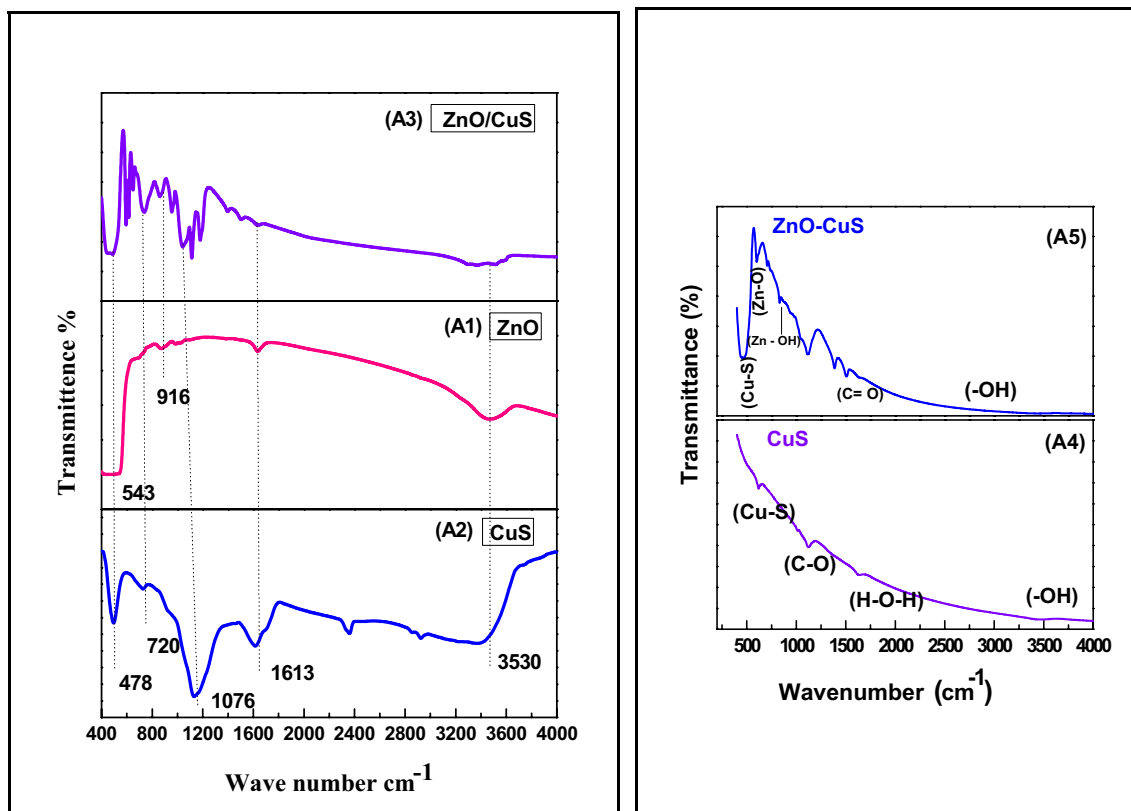
Fig. 7 FT-IR spectrum of A1, A2, A3, A4 and A5 nanoparticles

scattering of the incident light by the non-uniform surface of the nanocrystal. The absorption of the visible region has increased and thereby attributes to the narrow band gap of the ZnO/CuS nanocomposite. The emission range of 500–580 nm is credited to the band-edge emissions of CuS, the blue shift of the band-edge emission is due to the reduced CuS NPs size and complex defects present inside the nanostructures. The selective excitation of energy in the shell levels originates owing to the deep trap transition, which contributes to the emission peaks between 528 and 541 nm. The PL spectra of ZnO/CuS nanocomposite show luminescence at 439 nm. The broad visible emission band is mainly credited to the recombination of electrons caused by structured effects such as zinc vacancies, oxygen vacancies and interstitial oxygen. From the observations of both CuS and ZnO/CuS nanocomposites, we can see that the peak intensity increases and gradually becomes slender which may be caused by the electron transition from the localized level that is nearly below the conduction band to the valence band [29, 30].

3.8 Photocatalytic analysis

The photocatalytic performance of the prepared ZnO/CuS nanocomposites was done using mordant black 11 which was purchased from Sigma-Aldrich. 50 mL of 25 mg/l mordant black 11 dye was taken, and 10 mg of the prepared ZnO/CuS photocatalyst was dispersed in an aqueous solution using sonication for 12 h. Prior to irradiation, the mixture was stirred in dark so as to fix an adsorption equilibrium, and the photocatalytic degradation experiments were carried out for 150 min. The aliquot (3 ml) was drawn from the solution with a syringe after illumination at different time intervals and was centrifuged to remove the catalyst. The ZnO/CuS photocatalytic suspension was irradiated with a direct solar source, and all the experiments were conducted under similar conditions between 11:30 a.m. to 4:00 p.m. UV–Vis absorption spectra of the supernatant were then determined using a U-1800 UV–visible spectrophotometer.

The efficiency of decolorization (E) was calculated using the formula,

$$E = \left(1 - \frac{A}{A_0}\right) \times 100 \tag{3}$$

where A_0 stands for the absorbance at $t = 0$ min and A denotes the absorbance after complete degradation after $t = 150$ min.

The photocatalytic activity of the prepared catalyst was assessed under direct solar irradiation, 25 mg/l mordant
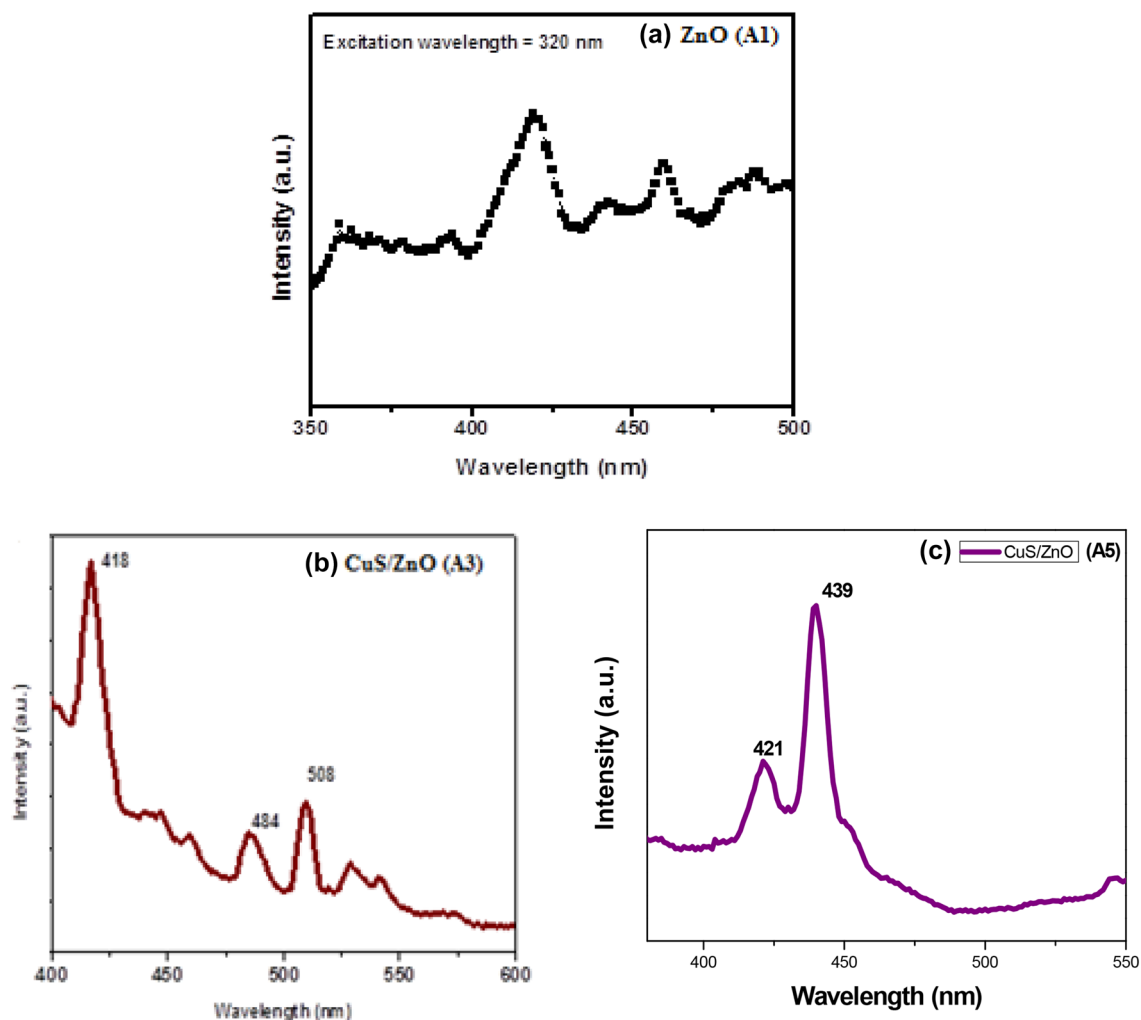
Fig. 8 Photoluminescence spectrum of **a** ZnO (A1) and **b**, **c** ZnO/CuS nanocomposites (A3 and A5)

black 11 which showed a major absorption band at around 527 nm was chosen as the representative hazardous dye. Just as Fig. 9b, the initial adsorption of the ZnO/CuS catalyst by the mordant black 11dye in the dark was noted before photocatalytic process. This proved the lack of adsorption capability for mordant black 1 dye. For a comparative analysis, a blank sample of mordant black 11 dye was kept under solar light without the addition of a catalyst, and the resultant photolysis of mordant black 11 was found to be extremely weak. Table 2 provides information about the corresponding values of the rate constant of ZnO (A1), ZnO/CuS (A3) and ZnO/CuS (A5) photocatalyst toward the degradation of the dye molecule. From Fig. 9a, it is clear that the highest rate constant was found for sensitized ZnO/CuS photocatalysts in comparison with ZnO nanoparticles. This could be associated with aggregation of nanoparticles onto the surface of ZnO, which attributes to the increase in diffusion length and probability of recombination of the light-induced electron–hole pairs, which in turn cuts down the injection rate

of photoelectrons in ZnO. While ZnO/CuS nanocomposite (A5) shows better performance which could be due to the uniform deposition of CuS nanoparticles over ZnO surface, thereby felicitating easier charge transport mechanism to precede the photocatalysis reaction. In Fig. 9, after 150 min of sunlight irradiation, about 90% of mordant black 11 could be degraded by the as-prepared ZnO. It was observed that when ZnO/CuS nanocomposites were used as photocatalysts, the photocatalytic efficiency was increased up to 97% in 150 min. Thus, the ZnO/CuS exhibited greater photocatalytic activity compared to the pure ZnO, indicating that photocatalytic activity has been improved when CuS was introduced. These enhancements is mainly attributed to the fact that the specific surface area of the ZnO/CuS (A5) is larger than that of pure ZnO and the reduction in photoinduced pair of electron–hole recombination.

The photocatalytic degradation of mordant black 11 dye was analyzed by the UV–vis absorption spectra using the catalysts such as pure ZnO nanoparticles and ZnO/CuS
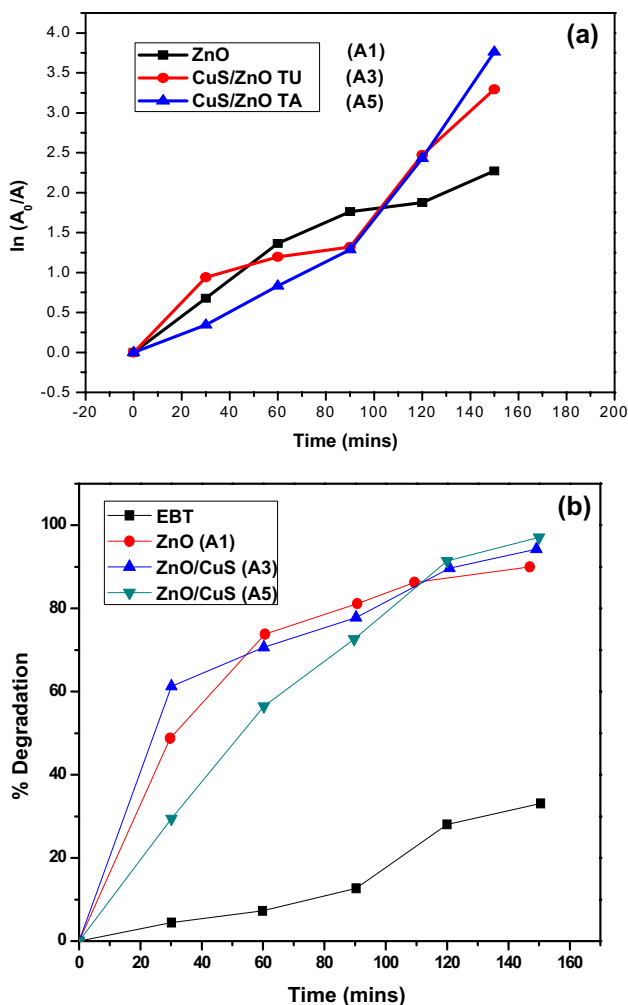
Fig. 9 **a** Determination of rate constants and **b** % degradation of mordant black 11 dye for different photocatalysts with respect to irradiation time under sunlight irradiation

Table 2 Tabular representation of rate constant values for ZnO (A1) and ZnO/CuS (A3 and A5)

Sample	Pseudo-first-order rate constant K min^{-1}	Maximum linear regression coefficient R^2	Degradation efficiency %
ZnO (A1)	0.02445	0.856	90
ZnO/CuS (A3)	0.0217	0.9016	94.29
ZnO/CuS (A5)	0.0283	0.6117	97.68

nanocomposites, which is shown in Fig. 10. The initial purple color of the solution turns light colored, by increasing the solar light irradiation time. Analyzing the degradation% evinced in Fig. 11, it can be observed that the photocatalytic activity of ZnO/CuS nanocomposite (A5) was higher than that of the as-prepared ZnO (A1).
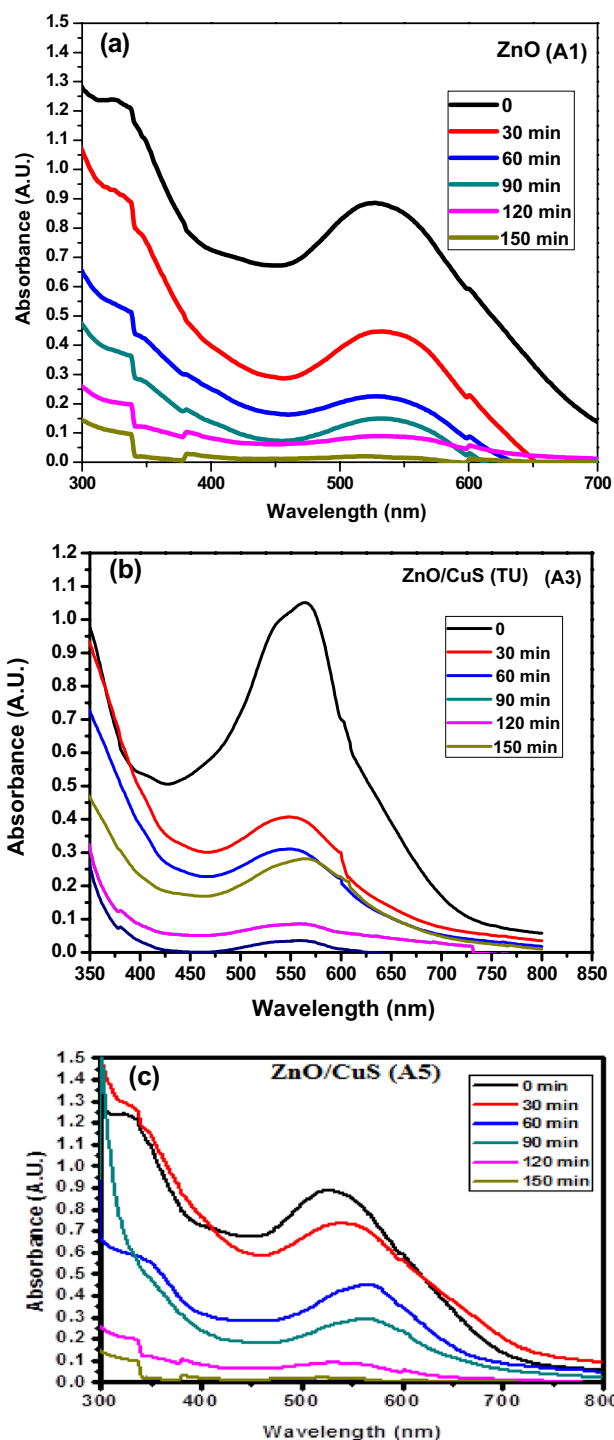

Fig. 10 UV–Vis absorbance spectra of degradation of mordant black 11 dye under sunlight irradiation of **a** ZnO and **b** ZnO/CuS (TU) and **c** ZnO/CuS (TA) nanocomposites

For the purpose of the further purification, it is imperative to check the long-term stability of the photocatalyst. Figure 11a, b shows the number of cycles for which ZnO and ZnO/CuS nanocomposites can be effectively used for the
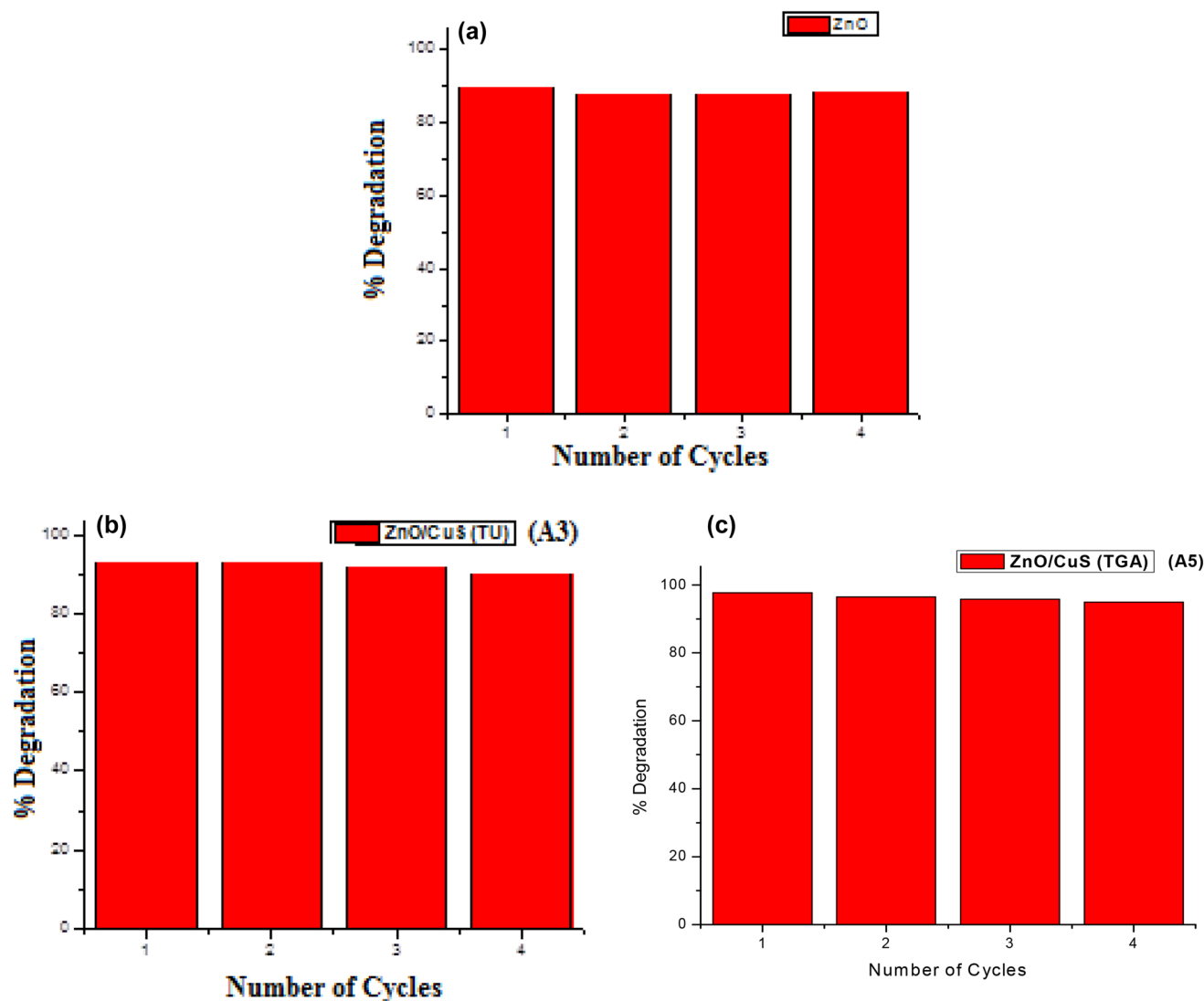
Fig. 11 **a–c** shows the reusability of ZnO (A1), ZnO/CuS (A3 and A5) nanocomposite for the photodegradation of mordant black 11 dye

degradation of mordant black 11 dye under direct sunlight. After the observation, it has been confirmed that the samples retained their good photocatalytic activity even after three cycles; therefore, their stability in the photodegradation process of organic pollutants is evident.

3.9 Mechanism of photocatalytic reactions

Under solar irradiation, electron–hole pairs are generated within CuS. The photogenerated electrons being minority carriers in p-type CuS effortlessly migrated to the conduction band of ZnO. On the other hand, since the valence band potential of CuS is greater than that of ZnO, and the holes stay on the surface of CuS. Similarly for ZnO, solar light excited electrons remain in the conduction band acting as electron reservoirs, whereas the holes (minority carriers) in

the valence band of ZnO migrate to the valence band of CuS. In this manner, CuS sensitized ZnO provides an easier pathway for separation of electron–hole pair generated in CuS and ZnO under sunlight irradiation. The proposed charge transport mechanism in CuS sensitized ZnO is depicted in Fig. 12

The physical process that occurs due to the presence of sensitized CuS/ZnO nanocomposite and mordant black 11 are provided below. During the sunlight exposure on the aqueous medium which contains the dye molecules and CuS/ZnO photocatalyst, the photogenerated electrons in conduction band (CB) of CuS nanoparticles are transferred to CB of ZnO, which are subsequently absorbed by dissolved oxygen in water to form superoxide radicals (O_2). These superoxide radicals further react with water molecules and finally for hydroxyl radicals (OH). Under the illumination of sunlight,
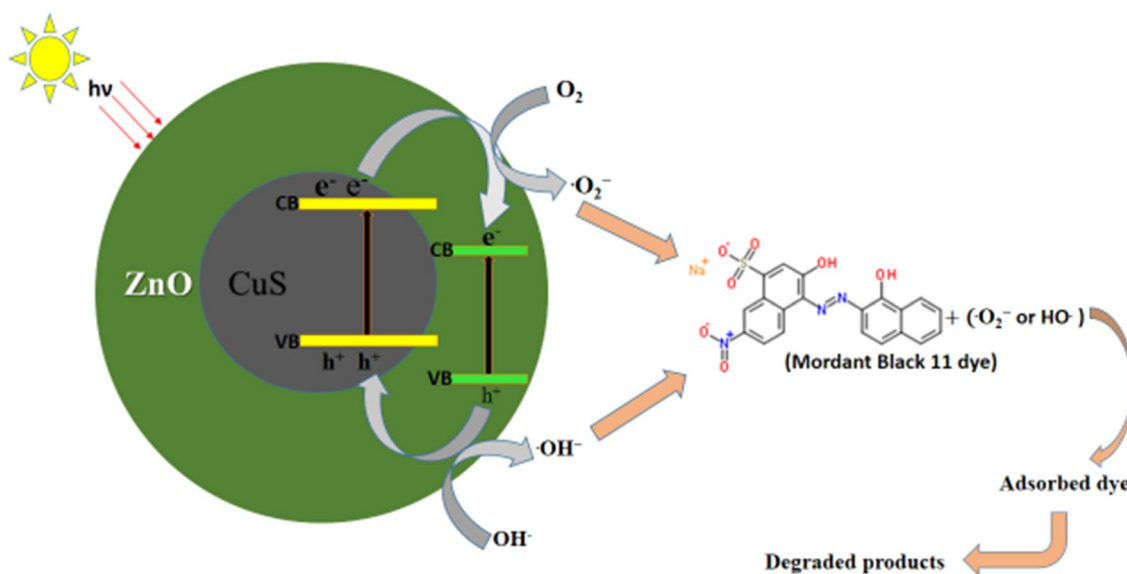
Fig. 12 Graphical representation of the ZnO/CuS nanocomposites

the holes migrated from the valence band of ZnO to that of CuS nanoparticles also form hydroxyl radicals. The dissolved oxygen and negatively charged hydroxyl radical in the water act as electron and hole scavengers in the process of electron–hole separation. Additionally, the presence of oxygen as electron scavengers prolongs the combination rate of electron–hole pairs. The presence of considerable amount of hydroxyl radicals (OH) easily oxidizes the organic dye molecules present in the aqueous solution, and also, the high oxidative potential of the holes in CuS/ZnO photocatalyst allows the explicit oxidation of dyes. Thus, it can be inferred from the obtained experimental results that the sensitized CuS/ZnO (A5) nanocomposite serves as a promising and cost-effective photocatalytic material in addition to the existing ones.

4 Conclusions

ZnO (A1), CuS (A2 and A4) and ZnO/CuS (A3 and A5) nanocomposite were prepared via facile hydrothermal route. The particle size derived from XRD was nearby to the value acquired from HRTEM analysis. The decreased band gap and large surface area of ZnO/CuS (A5) provide more surface active sites for the adsorption of the reactive molecules, and it is assessed to be apt and fruitful in the photocatalytic process. These significances evidence the improved photocatalytic performance of photocatalytic degradation of mordant black 11 dye. The photocatalytic activity of the ZnO/CuS (A5) nanocomposite prepared by using thioglycolic acid as the sulfur source exhibits greater degradation

efficiency with higher absorption ability when compared to ZnO (A1) and ZnO/CuS (A3) nanocomposite.

References

1. G. Murugadoss, J. Mater. Sci. Technol. **28**, 587–593 (2012)
2. M. Saranya, C. Santhosh, S. Prathap Augustine, A. Nirmala Grace, J. Exp. Nanosci. **9**, 329–336 (2014)
3. A. Naveed Ul Haq, A. Nadhman, I. Ullah, G. Mustafa, M. Yasinzai, I. Khan, J. Nanomater **2017**, 1–14 (2017)
4. B. Pejjai, M. Reddivari, T.R.R. Kotte, Mater. Chem. Phys. **239**, 122030 (2020)
5. F. Ghribi, A. Alyamani, Z. Ben Ayadi, K. Djessas, L. EL Mir, Energy Procedia **84**, 197–203 (2015)
6. M. Pal, N.R. Mathews, E. Sanchez-Mora, U. Pal, F. Paraguay-Delgado, X. Mathew, J. Nanopart. Res. **17**, 301 (2015)
7. S. Goel, Feng Chen, Weibo Cai. Small **10**, 631–645 (2014)
8. J. Xu, X. Cui, J. Zhang, H. Liang, H. Wang, J. Li, Bull. Mater. Sci. **31**, 189–192 (2008)
9. F.F. Castillón-Barraza, M.H. Farías, J.H. Coronado-López, M.A. Encinas-Romero, M. Pérez-Tello, R. Herrera-Urbina, A. Posada-Amarillas, Adv. Sci. Lett. **4**, 596–601 (2011)
10. U.T.D. Thuy, N.Q. Liem, C.M.A. Parlett, G.M. Lalev, K. Wilson, Catal. Commun. **44**, 62–67 (2014)
11. H.R. Ghorbani, F.P. Mehr, H. Pazoki, B.M. Rahmani, Orient. J. Chem. **31**, 1219–1221 (2015)
12. L. Zhu, M. Zheng, J. Lu, M. Xu, H.J. Seo, J. Nanomater. (2014)
13. G. Yang, W. Yan, Q. Zhang, S. Shen, S. Ding, Nanoscale **5**, 12432–12439 (2013)
14. X. Jiang, Yi Xie, Lu Jun, W. He, L. Zhu, Y. Qian, J. Mater. Chem. **10**, 2193–2196 (2000)
15. P. Lu, W. Zhou, Y. Li, J. Wang, Wu Ping, Appl. Surf. Sci. **399**, 396–402 (2017)
16. J. Yu, J. Zhang, S. Liu, J. Phys. Chem. B C **114**(32), 13642–13649 (2010)
17. M. Lee, K. Yong, Nanotechnology **23**, 194014 (2012)

18. Z. Liu, J. Han, Li Han, K. Guo, Y. Li, T. Cui, Bo Wang, X. Liang, Mater. Chem. Phys. **141**, 804–809 (2013)

19. Q. Cong, X. He, M. Gao, X. Ma, G. Li, Mater. Res. Innov. **18**, S4–740 (2014)

20. D. Hong, W. Zang, X. Guo, Y. Fu, H. He, J. Sun, L. Xing, B. Liu, X. Xue, ACS Appl. Mater. **8**, 21302–21314 (2016)

21. P. Kundu, P.A. Deshpande, G. Madras, N. Ravishankar, J. Mater. Chem. **21**, 4209–4216 (2011)

22. U. Shamraiz, R.A. Hussain, A. Badshah, J. Solid State Chem. **238**, 25–40 (2016)

23. M. Basu, N. Garg, A.K. Ganguli, J. Mater. Chem. **2**, 7517–7525 (2014)

24. A. Kołodziejczak-Radzimska, E. Markiewicz, T. Jesionowski, J. Nanomater. **2012**, 15 (2012)

25. S. Harish, M. Sabarinathan, J. Archana, M. Navaneethan, K.D. Nisha, S. Ponnusamy, V. Gupta et al., Appl. Surf. Sci. **418**, 147–155 (2017)

26. R. Sharma, F. Alam, A.K. Sharma, V. Dutta, S.K. Dhawan, J. Mater. Chem. **2**, 8142–8151 (2014)

27. H. Qu, L. Cao, Su Ge, W. Liu, R. Gao, C. Xia, J. Qin, J. Nanopart. Res. **16**, 2762 (2014)

28. Y. Zhang, B. Huang, P. Li, X. Wang, Y. Zhang, Tribol. Int. **58**, 7–11 (2013)

29. J. Varghese, K.T. Varghese, Mater. Chem. Phys. **167**, 258–264 (2015)

30. R. Ullah, J. Dutta, J. Hazard. Mater. **156**, 194–200 (2008)